1 Title page

2 Effect of colloidal particle size on physicochemical properties

3 and aggregation behaviors of two alkaline soils

4 Yu-yang Yan[1], Xin-ran Zhang[1], Chen-yang Xu[1,2]*, Jun-jun Liu[1], Fei-nan

5 Hu[3,4], Zeng-chao Geng[1,2]

6 (1. *College of Natural Resources and Environment*, *Northwest A&F University*,

7 *Yangling, Shaanxi 712100, China*; 2. *Key Laboratory of Plant Nutrition and the Agri-*

8 *environment in Northwest China, Ministry of Agriculture, Northwest A&F University,*

9 *Yangling, Shaanxi 712100, China; 3. State Key Laboratory of Soil Erosion and Dryland*

10 *Farming on the Loess Plateau, Northwest A&F University, Yangling, Shaanxi 712100,*

11 *China; 4. Institute of Soil and Water Conservation, Chinese Academy of Sciences,*

12 *Ministry of Water Resources, Yangling, Shaanxi 712100, China*)

14 ***Corresponding author:**

15 Chen-yang Xu

16 Email address: xuchenyang@nwafu.edu.cn, xuchenyang.ms@163.com;

17 Postal address: College of Natural Resources and Environment, Northwest

18 A&F University, No. 3 Taicheng Road, Yangling District, Shaanxi 712100,

19 China.

Abstract

Colloidal particles are the most active soil components, and they vary in elemental composition and environmental behaviors with the particle size due to the heterogenous nature of natural soils. The purposes of the present study are to clarify how particle size affects the physiochemical properties and aggregation kinetics of soil colloids, and to further reveal the underlying mechanisms. Soil colloidal fractions, from two alkaline soils—Anthrosol and Calcisol were subdivided into three ranges: $d < 2$ μm, $d < 1$ μm and $d < 100$ nm. The organic and inorganic carbon contents, clay mineralogy, surface electrochemical properties, including surface functional groups and zeta potentials, were characterized. Through time-resolved light scattering technique, the aggregation kinetics of soil colloidal fractions were investigated, and their critical coagulation concentrations (CCCs) were determined. With decreasing colloidal particle diameter, the total carbon content, organic carbon, organic functional groups content and illite content all increased. The zeta potential became less negative and the charge variability decreased with decreasing particle diameter. The CCC values of Anthrosol and Calcisol colloids followed the descending order of $d < 100$ nm, $d < 1$ μm, $d < 2$ μm. Compared with the course factions ($d < 1$ μm and $d < 2$ μm), soil nanoparticles were more abundant in organic carbon and more stable clay minerals ($d < 100$ nm), thus they exhibited strongest colloidal suspension stability. The differences in organic matter contents and clay mineralogy are the fundamental reasons for the differences in colloidal suspension stability behind the size effects of Anthrosol and Calcisol colloids. The present study revealed the size effects of two alkaline soil colloids on carbon content, clay minerals,

42 surface properties and suspension stability, emphasizing that soil nanoparticles are

43 prone to be more stably dispersed instead of being aggregated. These findings can

44 provide references for in-depth understanding of the environmental behaviors of the

45 heterogeneous soil organic-mineral complexes.

46 **Keywords:** Nanoparticles; Clay mineral composition; zeta potential; Critical

47 coagulation concentration

1. Introduction

Soils contain a series of solid particles in continuous sizes, ranging over six orders of magnitude from nanometers to millimeters (Lead and Wilkinson, 2006; Li et al., 2011), among which soil colloids are the most reactive fractions. Soil colloids are characterized by high surface area and abundant surface charges, exhibiting high potential for carbon sequestration and strong adsorption capacity, which can largely determine the fate and transport of pathogens, nutrients, heavy metals and organic pollutants, and might cause environmental problems to adjacent water bodies or groundwater (Baalousha et al., 2009; Calabi-Floody et al., 2011). Due to their high reactivity and fluidity in aqueous environment, soil colloids play an important role in physical, chemical and biogeochemical processes in natural environment (Schäfer et al., 2012; Mayordomo et al., 2016). The capacity of soil colloids in mobilizing bound nutrients and pollutants is closely related to their dispersion stability under various environmental conditions (Won and Burns, 2018). Therefore, studies on the dispersion stability of soil colloids have attracted extensive attention.

Currently, the definition of soil and environmental colloidal fractions is ambiguous. Soil colloidal fractions are defined as soil particles in diameter of < 1 μm (Lead and Wilkinson, 2006; Weil and Brady, 2016), and also being of < 2 μm (Zhang et al., 2021); while in some extreme cases, they can refer to the particles in diameter of 5–10 μm (Yin et al., 2010). Such discrepancies are seen among publications due to the fact that colloids are defined based on the particle diameter range within which they can display colloidal properties. Since for different materials, e.g., metal (Fe/Al/Ti) oxides, silica

70   gel, phyllosilicates, the specific colloidal range differs greatly.

71   Compared with engineered nanoparticles with known mineralogical organization,

72   natural soils are much more heterogeneous (Cárdenas et al., 2010); their elemental

73   composition and clay mineralogy of soil colloids change with particle size. Tsao et al.,

74   (2013) found that quartz and feldspar were mainly dominant in colloidal particles of <

75   2 μm and 450–2000 nm in red soil (Ferralsols, WRB, IUSS Working Group WRB.

76   2022), while illite and montmorillonite were the main clay minerals in nanoparticles

77   (1–100 nm). In addition, the mineral structure at nanometer scale also changes.

78   Compared with colloidal particles of < 2 μm, the Si/Al ratio in nanoparticles increased,

79   and the surface area, morphology, crystallinity, surface atomic structure and frame

80   structure were significantly different (Tsao et al., 2011). Furthermore, particle size also

81   affects the surface potential of soil colloids. Tang et al., (2015) investigated the surface

82   potential variations with particle size (1–10 μm, 0.5–1 μm, 0.2–0.5 μm, < 0.2 μm) for

83   variably-charged yellow soil (Lixisols) and permanently-charged purple soil

84   (Leptosols); among the colloidal fractions, the absolute surface potential of the finest

85   particles of purple soil (Leptosols) was lowest while that of the yellow soil (Lixisols)

86   was the largest, caused by the differences in surface charge density. Thus, the influences

87   of particle size on elemental composition and surface properties of soils should be

88   further studied.

89   In recent years, great progress has been made in the study of dispersion stability

90   of soil clay minerals, such as montmorillonite, kaolinite, illite or hematite, and soil

91   nanoparticles (Xu et al., 2018; Sun et al., 2020; Wei et al., 2021; Zhu et al., 2014). He

92 et al., (2008) demonstrated that hematite nanoparticles with various particle diameters

93 showed different surface properties and aggregation behaviors under the same pH

94 conditions; moreover, the critical coagulation concentrations (CCCs) of hematite

95 decreased with the decrease of particle diameter. Zhou et al., (2013) compared the

96 CCCs of ten different TiO_2 nanoparticles with varying sizes and indicated that crystal

97 structure and particle diameter both affected the aggregation behaviors of TiO_2. Zhang

98 et al. (2016) confirmed that the types of clay minerals for two Alfisols changed from

99 smectite and vermiculite to kaolinite and illite when the particle size varied from

100 colloids to nanoparticles. Therefore, the dependence of physiochemical properties,

101 surface properties and environmental behaviors on particle size for heterogeneous soil

102 colloidal particles needs systematic investigation.

103   In the present study, soil colloidal particles of two alkaline soils—Anthrosol sand

104 Calcisols were subdivided into three ranges: $d < 2$ μm, $d < 1$ μm and $d < 100$ nm. Their

105 organic fraction and clay mineralogy, surface electrochemical properties and colloidal

106 stability were studied. This study selected two representative calcareous soils to verify

107 the following scientific hypothesis: soil colloids are organic-inorganic composites. As

108 particle diameter decreases (from colloid particles to nanoparticles), the number of

109 organic functional groups on the surface of soil colloids increases, and the type of clay

110 minerals shifts towards finer clay particles, e.g. illite, resulting in increased specific

111 surface area and decreased charge density, and thus enhanced suspension stability,

112 meaning particle diameter influences the composition of soil colloidal fractions,

113 thereby changing surface properties and suspension stability. The findings can have

important implications for predicting the environmental performances of colloids and colloid-facilitated nutrients, pollutes and pathogens in natural soil and water environment.

2. Materials and methods

2.1 Soil sampling

The study collected two surface soil samples (0–20 cm), Lou soil and Cinnamon soil, being the most common and characteristic calcareous soils, by mixing soils form 5–10 sampling points using a stainless-steel auger at Yangling District (N38°18′14″ and E108°2′30″), and Zhouzhi Country (N34°8′8″ and E108°3′10″), on the Guanzhong Plain, Shaanxi province, northwest China, respectively. Among these, Lou soil, as a unique calcareous soil, have formed on the basis of cinnamon soil through long-term anthropogenic maturation. According to World Reference Base for Soil Resources (WRB, IUSS Working Group WRB. 2022), the Lou soil and Cinnamon soil are classified as Calcic Protocalcic Calcisols (Loamic, Lixic, Humic) and Hortic Endoanthric Anthrosols (Loamic, Luvic, Eutric, Calcic), respectively. Both types of soil developed from loess parent material. The typical soil profile configuration for the tested Anthrosols is Ap1-Ap2-Bt-Bk-C, while for the Calcisols, it is Ah-Bt-Bk-C.

Soils samples were taken back to the laboratory for air-drying and sieving. The basic soil properties were determined based on standard methods. Soil pH was measured with a pH electrode, employing a solution-to-soil ratio of 2.5:1. Soil organic carbon (SOC) was determined using the $K_2Cr_2O_7$ oxidation method. The cation exchange capacity (CEC) of soil was measured with exchange method. The $CaCO_3$

136 content was determined by gasometric method. The free Fe/Al oxides were extracted

137 by dithionite-citrate-bicarbonate (DCB) solution. The particle size distribution was

138 measured using the laser diffractometer of Malvern Mastersizer 2000 (Malvern

139 Instruments Ltd., UK). The pH of Anthrosols was 8.34 while it was 8.32 for Calcisols.

140 The SOC of Anthrosols and Calcisols were 7.25 $g \cdot kg^{-1}$ and 9.22 $g \cdot kg^{-1}$, respectively.

141 The CEC of Anthrosols and Calcisols were 25.9 $cmol \cdot kg^{-1}$ and 22.2 $cmol \cdot kg^{-1}$.The

142 contents of $CaCO_3$ in Anthrosols and Calcisols were 51.7 $g \cdot kg^{-1}$ and 82.5 $g \cdot kg^{-1}$. The

143 Free Fe/Al oxides content of Anthrosols and Calcisols were 22.8 $g \cdot kg^{-1}$ and 23.1 $g \cdot kg^{-1}$.

144 The proportions of Sand (2–0.02 mm), Silt (0.02–0.002 mm) and Clay (<0.002 mm) in

145 Anthrosols were 34.0%, 40.6% and 25.4% while those were 28.0%, 44.8% and 27.2%

146 for the Calcisols.

147 **2.2 Extraction of soil colloidal fractions in different size ranges**

148 The soil colloidal particles were extracted based on the Stokes' law, and detailed

149 procedures can be found in our previous publication (Hu et al., 2022). Briefly, 50 g of

150 dry soil was weighed into a beaker containing 500 mL of distilled water, and put the

151 suspension under sonication for an hour using the ultrasonic cell disrupter (XO-900D,

152 Nanjing Xianou Instruments Corporation, China) while maintaining the temperature

153 below 30°C. Afterwards, the suspension was transferred to a larger beaker and distilled

154 water was added to make up the total volume of 5 L. The suspension was further

155 dispersed using an electronic blade stirrer (JB-200, Shanghai Nanhui Huiming

156 Apparatus, China) for one hour, before being sieved through sieve with a pore size of

157 53 μm, and the upper suspensions containing soil colloidal particles in different

diameters were collected by centrifugation. Based on the equation (1), centrifugation

speed and time for colloidal particles of $d < 2$ μm, < 1 μm and < 100 nm were calculated

and shown in Table S1.

$$t = \frac{\eta \lg \frac{R_2}{R_1}}{3.81 N^2 r^2 \Delta d} \qquad (1)$$

in which, t is time for centrifugation (s); R_1 is the distance from the surface of the liquid

to the center of the axis of the centrifuge, here is 5.7 cm; R_2 is distance from the particles

to the center of the axis of the centrifuge, here is 10.5 cm; N (rev·s^{-1}) is the centrifuge

speed; r (cm) is the desired colloidal particle radius; Δd is the difference in density

between the soil particles (2.65 g·cm^{-3}) and water (1 g·cm^{-3}), while Δd is 1.65 g·cm^{-3};

η is the water viscosity coefficient, here is 0.00839 g·cm^{-1}·s^{-1} at 25 °C.

2.3 Characterization of soil colloidal fractions in different size ranges

The initial particle diameters of soil colloids were determined by a time-resolved

dynamic light scattering (DLS) apparatus (Nanobrook Omni, Brookhaven, USA), each

sample was measured 15 times to get the initial particle diameters. The organic carbon

contents in soil colloids were determined by potassium dichromate external heating

method and total carbon content was determined by elemental analyzer (Elementar

Vario EL III, Germany). Total carbon and organic carbon are the averaged results of 3

measurements each. The inorganic carbon content was calculated by subtraction

method (Wang et al., 2011). The clay mineralogy of soil colloids was determined by the

XRD (Ultima-IV, Rigaku, Japan), and by comparing the intensity of the dominant X-

ray diffraction peak of the soil mineral colloid to a standard mineral reference (Database

179   ICDD 2004), the relative percentage content of the minerals was determined. The

180   specific surface areas of the soil colloids were measured by BET-N_2 method (ASAP

181   2460, Micromeritics instrument, USA). High-resolution spectra of C1s and O1s of soil

182   colloids were acquired by X-ray photoelectron spectroscopy (XPS) (Thermo Scientific

183   K-Alpha, USA) (Luo et al., 2019), and the Gaussian−Lorentzian curve-fitting program

184   (XPSPEAK 4.1) was used to analyze the XPS spectra. The zeta potentials of soil

185   colloids were measured by Zeta PALS equipped with a BI-ZTU Autotitrator (ZetaPALS,

186   Brookhaven, USA) with 1 mmol·L^{-1} NaCl solution as the background electrolyte, and

187   the pH range of colloidal suspension was set to 3–10 adjusted with 0.1 mol·L^{-1} HCl

188   and NaOH. Each sample was measured six times to get the average zeta potential values.

189   The concentrations of K^+, Na^+, Ca^{2+}, and Mg^{2+} in soil colloidal suspensions were

190   measured by flame atomic absorption spectrophotometry (PinAAciie 900F, USA).

191   **2.4 Aggregation kinetics of soil colloidal fractions**

192   The aggregation kinetic curves of soil colloidal particles in different electrolytes

193   were determined by time-resolved DLS measurements. The incident wavelength was

194   635 nm and the scattering angle was 90°. The stock colloidal suspensions with particle

195   concentration of 200 mg·L^{-1} were mixed with electrolyte solutions with equal volume.

196   The suspension pH was adjusted to 8.0, which was close to the pH value of natural soil

197   with addition of 0.1 mol·L^{-1} HCl or NaOH before measurement. The chosen electrolyte

198   concentrations for NaCl and $CaCl_2$ were 200–2000 and 2–20 mmol·L^{-1}. The effective

199   diameter (D_h) of the mixed sample was automatically recorded every 2 min, and an

200   aggregation kinetic curve was obtained in 30 min monitoring. According to generally

201 adopted by most research, the aggregation curve was determined only for one time

202 without repetition (Chen and Elimelech, 2006; Mashayekhi et al., 2012; Zhu et al., 2014;

203 Liu et al., 2018).

204 **2.5 Calculation of critical coagulation concentration**

205   According to the particle interaction theory, the aggregation kinetic curves under

206 electrolyte conditions can be divided into reaction-limited aggregation (RLA) stage

207 under low concentration which was affected by electrolyte conditions and diffusion-

208 limited aggregation (DLA) stage under high concentration which was not affected by

209 electrolyte concentration. The CCC is the critical electrolyte concentration when the

210 aggregation process changes from the RLA state ($\alpha < 1$) to the DLA state ($\alpha = 1$).

211 Attachment efficiency (α) represents the bonding probability of particle collisions and

212 can be calculated for each electrolyte concentration by using equation 2, which allowed

213 the curve of α as a function of electrolyte concentration to be plotted (Xu et al., 2020a;

214 Hu et al., 2022).

215
$$\alpha_{\mathrm{exp}} = \frac{1}{W} = \frac{k_{11}}{\left(k_{11}\right)_{fast}} = \frac{\frac{1}{N_0}\left(\frac{\mathrm{d}a_h(t)}{\mathrm{d}t}\right)_{t\to 0}}{\frac{1}{\left(N_0\right)_{fast}}\left(\frac{\mathrm{d}a_h(t)}{\mathrm{d}_t}\right)_{t\to 0, fast}} \tag{2}$$

216 where D_h is the effective diameter of particles, t is the time (min); N_0 is the density of

217 particles; K_{11} is the aggregation rate of RLA; $(K_{11})_{fast}$ is the aggregation rate of DLA.

218 The intersection of RLA regime and DLA regime is the CCC.

219   The aggregation rates were calculated by the average of the last 5 effective

220 diameters divided by the aggregation time at specific electrolyte concentration. The

221 fractal dimension in the DLA regime was obtained based on the method proposed by

222 Wang et al. (2013).

223
$$D(t) = b * t^n + D_0 \tag{3}$$

224 in which, $D(t)$ is the colloidal effective diameter at time t (min), D_0 is the initial effective

225 diameter of colloids, and b and n are constants determined by the aggregation curves.

226 The fractal dimension is $d_f = 1/n$ in the DLA regime.

3. Results and discussion

3.1 Particle size and distribution characteristics of Anthrosol and Calcisol
colloidal fractions

230 The average diameters of Anthrosol and Calcisol colloids were measured by time-

231 resolved DLS, and the results were shown in Table 1. The number-weighted diameters

232 for Anthrosol colloids of $d < 2$ μm were about 1.04 times of $d < 1$ μm, and about 1.84

233 times of d < 100 nm, respectively. The intensity-weighted diameters for Anthrosol

234 colloids were 294.10~396.81 nm. For Calcisol colloidal fractions, the number-weighted

235 diameters for colloids of $d < 2$ μ m were about 1.07 times of $d < 1$ μ m, and about 1.65

236 times of d < 100 nm, and the intensity-weighted diameters were 312.25~439.20 nm.

237 The intensity-weighted diameters were generally higher than the number-weighted

238 diameters, especially in polydisperse system (Xu et al., 2020b). The colloidal particles

239 in the soil solution were in constant Brownian motion, upon illumination by light, these

240 colloidal particles scatter light, causing variations in light intensity. This phenomenon

241 allowed for the calculation of the effective diameter of the particles, which was the

242 intensity-weighted diameter (Filella et al., 1997). Given that particle diameter is

proportional to the sixth power of light intensity. Consequently, in polydisperse systems where larger particles were present, the number-weighted diameter provided typically a more accurate representation of the true diameter of colloidal particles (Xu et al., 2015).

(Insert Table 1 near here)

From table 1, it can be seen that the average colloidal diameters of $d < 2$ μm were close to that of $d < 1$ μm, and they were both significantly higher than that of the nano-sized fraction. From the particle size distribution characteristics, it is clear that the size range indicated by the differences of D_{90} and D_{10} increased with intended particle diameter. For Anthrosol and Calcisol, 74.69% and 63.55% of all particles contained in the colloidal suspensions of $d < 100$ nm were actually less than 100 nm, respectively, indicating the complexity of soil colloidal particle irregularity.

3.2 Physiochemical properties and clay mineralogy of Anthrosol and Calcisol colloids

Table 2 shows the physiochemical properties of soil colloidal fractions. The yields of each colloidal fraction of Anthrosol were slightly larger than that of Calcisol, respectively. The yields of colloidal particles of $d < 2$ μm were about 1.3~1.4 times of $d < 1$ μm, and about 4.0~4.9 times of $d < 100$ nm, respectively. With the decreasing colloidal particle diameter, the total carbon content, organic carbon and inorganic carbon content all increased, suggesting the finer particles were richer in carbon. This tendency is in agreement with other publications (Zhang et al., 2021; Said-Pullicino et al., 2021; Hu et al., 2022). The specific surface areas for colloidal fractions of $d < 1$ μm

265   were largest of all, which may be related to the structures of formed clusters while

266   drying the samples for observation under microscopy (Yu et al., 2017; Weissenberger

267   et al., 2021). Furthermore, Anthrosol and Calcisol nanoparticles exhibited the lowest

268   specific surface area. This phenomenon raised from Organic substances adsorb

269   relatively little inorganic nitrogen (Li et al., 2013; Wilson et al., 2008). Therefore,

270   However, to our knowledge, no other better method has been reported for measuring

271   the specific surface area of natural nanoparticles.

272   (*Insert Table 2 near here*)

273   The clay mineralogy of Anthrosol and Calcisol colloidal fractions is shown in

274   Table 3. Calcisol colloidal fractions were dominant by illite, kaolinite and chlorite while

275   there was less chlorite in Anthrosol colloidal fractions. With the decrease of particle

276   size, the content of illite increased and kaolinite content decreased. This tendency is in

277   agreement with other publications (Chenu and Plante, 2006; Zhang et al., 2016). Among

278   the dominant clay types, the size of illite is finer than kaolinite and chlorite (Weil and

279   Brady, 2016), so its mass percentage was higher in the nano-sized fraction.

280   (*Insert Table 3 near here*)

281   **3.3 Surface properties of Anthrosol and Calcisol colloids**

282   The XPS spectra of soil colloidal fractions are shown in Fig. 1. From Fig. 1, it can

283   be seen that the main C-containing functional groups were C–C/C-H/C=C, C–O, C=O,

284   and COO- groups at 284.6, 286.2, 288.0 and 289.4 eV, respectively (Liang et al., 2020;

285   Ding et al., 2023). The functional groups for colloidal particles of $d < 100$ nm were

286   more abundant than those for colloids of $d < 2$ μm and $d < 1$ μm, while there were no

287   significant differences between colloids of $d < 2$ μm and $d < 1$ μm. With the decrease

288   of colloidal particle diameter, the relative contents of oxygen-containing functional

289   groups (C–O, C=O, COO-) gradually decreased. Specifically, the content decreased

290   gradually from 32.01% in Lou colloids of $d < 2$ μm to 20.93% in Lou colloids of $d <$

291   100 nm (Table S2). The functional groups of C–O and COO- gradually decreased until

292   they eventually disappeared, more C=O groups were exposed to the surrounding air.

293   For Calcisol colloids (Fig. 1d, e, f), the relative contents of organic oxygen-

294   containing functional groups for colloidal particles of $d < 2$ μm, $d < 1$ μm and $d < 100$

295   nm showed a different trend, compared with that in Anthrosol colloids. The relative

296   contents of organic oxygen-containing functional groups gradually increased with the

297   decrease of diameter. This trend was particularly pronounced in fraction of $d < 100$ nm,

298   and contents of C–O and COO- were highly increased (Table S2).

299   (*Insert Figure 1 near here*)

300   Oxygen-containing functional groups of C–O, C=O and COO- are electronegative

301   functional groups, hydroxyl and carboxyl groups can lose protons and make the surface

302   of soil colloidal particles carry negative charges (Audette et al., 2021). Functional

303   groups of C–O, C=O and COO- can affect the negative charges carried on the colloidal

304   surface by forming hydrogen bonds, and their polarity can also affect the negative

305   charges on the surface when O atom combines with C and H. The electrons will lean

306   towards the O atom with stronger electronegativity, which also makes the colloidal

307   surface carry negative charges (Tan et al., 2019). The contents and types of oxygen-

308   containing functional groups are one of the main factors affecting colloid charge and

309   aggregation.

310   The zeta potential values of different colloidal fractions at the pH range of 3–10

311 are shown in Fig. 2. Zeta potentials of the colloidal particles were negative, indicating

312 that they were negatively-charged. The zeta potentials of Anthrosol and Calcisol

313 colloidal particles were more negative with increasing solution pH, due to the

314 deprotonation of the surface (Moayedi and Kazemian, 2013; Dong et al., 2019).

315 Compared with the Calcisol colloids, the zeta potentials of Anthrosol colloidal particles

316 were more negative, due to Anthrosol possessed a higher surface charge density. For

317 Calcisol colloids, the differences among colloidal fractions were larger.

318   (*Insert Figure 2 near here*)

319   In general, zeta potential became more negative with increasing particle diameter.

320 When the pH changed from 3 to 10, for every pH unit increased, the zeta potential

321 values of Anthrosol colloids of $d < 2$ μm, < 1 μm, and < 100 nm would be increased by

322 2.14 mV, 2.09 mV and 1.89 mV; and for Calcisol colloids, those variation rates were

323 2.15 mV, 1.45 mV and 1.37 mV, respectively. Those data demonstrate that the charge

324 variability decreasing with the decreasing particle diameter. Song et al., (2019)

325 compared the zeta potential of wheat straw biochar nanoparticles (< 100 nm) and

326 colloidal particles (< 1000 nm), and found that the absolute values of colloidal particles

327 were larger at same pH, which was explained by the differences in the number of

328 surface carboxyl and hydroxyl groups. The zeta potential of colloidal particles is

329 proportional to charge density, which means that it is related to both charge quantity

330 and specific surface area (Hou et al., 2009). Therefore, the size effect of zeta potential

331 of Anthrosol and Calcisol colloidal particles is mainly related to the reduction of charge

332 density caused by larger specific surface area of nanoparticles (Xu et al. 2020b).

3.4 Aggregation kinetics curves of Anthrosol and Calcisol colloids in NaCl and CaCl$_2$ solutions

The aggregation kinetics of Anthrosol and Calcisol colloids in NaCl and CaCl$_2$ solutions are shown in Figs. S1 and S2. The aggregation process of soil colloids was divided into RLA and DLA stages. The RLA stages for Anthrosol colloids of $d < 2$ μm, $d < 1$ μm and $d < 100$ nm in NaCl solution were 0–80, 0–80 and 0–100 mmol·L^{-1}, respectively, during which repulsive forces existed between the particles and attachment did not occur on every collision. As the electrolyte concentration continued to increase, the solution entered into the DLA regime. At this point, attachment occurred with every collision between particles, and the aggregation rates were not affected by the electrolyte concentration. At last, the effective diameters of the formed clusters were stable at around 1600 nm. Figure S1b, d and f showed that the aggregation behaviors of Anthrosol colloids in CaCl$_2$ solution were similar to that in NaCl solution, and the corresponding CaCl$_2$ concentrations for Anthrosol colloids of $d < 2$ μm, $d < 1$ μm and $d < 100$ nm in RLA stage were about 0–1.5, 0–1.5 and 0–2 mmol·L^{-1}, respectively.

The aggregation kinetics of Calcisol colloids in NaCl and CaCl$_2$ solutions were similar to Anthrosol colloids (Fig. S2). The RLA stages for Calcisol colloids of $d < 2$ μm, $d < 1$ μm and $d < 100$ nm in NaCl solution were 0–100, 0–120 and 0–250 mmol·L^{-1}, and were about 0–1.8, 0–1.7 and 0–2 mmol·L^{-1} in CaCl$_2$ solution, respectively. The effective diameters of the clusters for Calcisol colloids were stabilized at about 1600 nm and 1800 nm in NaCl and CaCl$_2$ solutions, respectively.

Aggregation rates of soil colloids varied with particle diameters at the same

355 electrolyte concentration, which was particularly evident in RLA stage (Table 4). With

356 decreasing particle diameter, the aggregation rates of Anthrosol and Calcisol colloids

357 in 50 mmol·L^{-1} NaCl and 1 mmol·L^{-1} CaCl$_2$ solutions exhibited a corresponding

358 decline. In addition, in 50 mmol·L^{-1} NaCl solution, the aggregation rates for Anthrosol

359 colloids of $d < 2$ μm, $d < 1$ μm and $d < 100$ nm were about 2.17, 2.09 and 1.95 times

360 those of Calcisol colloids, while the aggregation rates were about 1.46, 1.57 and 1.91

361 times those of Calcisol colloids in 1 mmol·L^{-1} CaCl$_2$ solution, respectively. Therefore,

362 from table 4, the aggregation rates of Anthrosol and Calcisol colloids showed the size

363 effect. From table 4, it could be observed that the fractal dimensions in NaCl solutions

364 were largely higher than those in CaCl$_2$ solutions, suggesting a much denser structure

365 (Meng et al., 2013). In other words, the formed structures in divalent solutions were

366 more open.

367 *(Insert Table 4 near here)*

368 **3.5 Suspension stability of Anthrosol and Calcisol colloids in NaCl and CaCl$_2$**

369 **solutions**

370 The CCCs for Anthrosol colloids of $d < 2$ μm, $d < 1$ μm and $d < 100$ nm in NaCl

371 solution were 80.40, 91.78 and 134.96 mmol·L^{-1}, respectively (Fig. 3a), and those for

372 Calcisol colloids were 121.10, 126.50 and 292.86 mmol·L^{-1}, respectively (Fig. 3b). The

373 CCCs increased with the decreasing particle diameter, indicating that the suspension

374 stability of soil nanoparticles was stronger than those of colloidal particles.

375 *(Insert Figure 3 near here)*

376 In CaCl$_2$ solutions, the CCCs for Anthrosol colloids of $d < 2$ μm, $d < 1$ μm and d

377   < 100 nm were 1.61, 1.68 and 1.77 mmol·L^{-1}, respectively, and for Calcisol colloids,

378   those corresponding values were 1.90, 1.91 and 2.13 mmol·L^{-1} (Fig. 4). The CCCs in

379   CaCl$_2$ solutions also increased with the decreasing particle size. The contents of K$^+$,

380   Na$^+$, Ca^{2+} and Mg^{2+} in Anthrosol and Calcisol colloidal suspensions decreased with the

381   decreasing colloidal particle diameter (Table S3), which was mainly due to the dilution

382   effect during the extraction process. Furthermore, Table S3 showed that the soluble

383   cation contents were rather low, and their effects on the CCCs of soil colloids could be

384   neglected.

385   (*Insert Figure 4 near here*)

386   Based on Figs. 3 and 4, 3 mmol·L^{-1} CaCl$_2$ solution could cause fast aggregation

387   of soil colloidal particles, while it required at least 80 mmol·L^{-1} NaCl solution for

388   comparable aggregation rate, indicating that the shielding effect of divalent cations on

389   negative charges of colloids was stronger than that of monovalent cations. The

390   quantitative calculation results showed that the CCC ratios of monovalent ion and

391   divalent ion system were between 25.64 and 27.09, which conformed to the Schulze-

392   Hardy rule (Baalousha, 2017).

393   For each type of the soil colloids, the higher the absolute zeta potential values of

394   colloidal particles, the more negative charges carried on the surface, and the higher the

395   stability (CCCs) of suspension. For the same particle diameter, e.g. *d* < 100 nm, the

396   absolute zeta potentials of Anthrosol colloids were larger (Fig. 2) while the

397   corresponding CCC was lower (Figs. 3 and 4). Study on the stability of biochar

398   nanoparticles showed that the absolute values of zeta potentials could not be used to

399   directly explain the stability difference among biochar nanoparticles from different

400   feedstock materials but could explain the influences of solution conditions on the

401   stability of biochar nanoparticles derived from the same feedstock material (Xu et al.,

402   2020a).

403   The CCCs of Anthrosol and Calcisol colloids increased with decreasing diameter;

404   that is, the CCCs of Anthrosol and Calcisol colloids both showed the size effects. Hsu

405   and Kuo (1995) demonstrated that the CCCs would generally decrease with the

406   increasing particle diameter because smaller particles possess thicker double electric

407   layers and higher electrolyte concentration is needed to neutralize charges on the

408   surface, which were consistent with the results of Anthrosol and Calcisol colloids. The

409   above explanation by Hsu and Kuo (1995) was derived from homogenous particles

410   whose composition does not change with particle diameter. The results of this paper

411   show that, for those two alkaline soils being such heterogeneous materials, when the

412   organic matter contents and mineral types changed with colloidal particle diameter, the

413   CCCs in monovalent and divalent solutions also decreased with increasing particle

414   diameter.

415   In this paper, the organic matter contents of soil nanoparticles were the highest, so

416   the CCCs were the largest, which were 1.7 and 2.4 times of the corresponding colloidal

417   particles of $d < 2$ μm. The suspension stability of different clay minerals has been

418   reported to vary with the mineralogical structure. The CCC of illite (≈ 100 mM) in

419   NaCl solution was significantly higher than that of kaolinite (≈ 20 mM) (Jiang et al.,

420   2012; Xu et al., 2017), indicating that the stability of illite suspensions is significantly

421 higher than that of kaolinite. So another possible reason for the higher stability of soil

422 nanoparticles is the increase of illite content and the decrease of kaolinite content.

423 Therefore, the differences in organic matter contents and clay mineralogy are the

424 fundamental reasons for the differences in colloidal suspension stability behind the size

425 effects of Anthrosol and Calcisol colloids.

4. Conclusion

427   This study obtained soil colloidal fractions with three different particle sizes from

428 Anthrosol and Calcisol using high-speed centrifugation and revealed the particle size

429 effects on the soil constitutes, surface properties, and aggregation behavior of

430 heterogeneous soil colloids. The results showed that, compared to coarse colloids ($d <$

431 2 μm and $d < 1$ μm), the organic carbon contents of Anthrosol and Calcisol

432 nanoparticles were higher, at 27.38 g·kg^{-1} and 28.31 g·kg^{-1}, respectively,

433 approximately twice and three times that of the coarse colloids and the bulk soils,

434 indicating that nanoparticles exhibit a strong potential for carbon sequestration. The

435 absolute zeta potential values of soil nanoparticles decreased with decreasing average

436 particle diameter, indicating a reduction in charge density. Anthrosol and Calcisol

437 nanoparticles exhibited greater suspension stability in NaCl and CaCl$_2$ solutions. On

438 one hand, this was due to the increased thickness of the double electric layer on the

439 surface of soil nanoparticles, resulting in stronger repulsive forces between particles;

440 on the other hand, it was due to the presence of more illite, which has higher CCC

441 compared to other clay minerals. In conclusion, for such a highly heterogeneous system

442 as soil, the size effects on soil colloidal suspension stability are strongly influenced by

variations driven by essentially mineral composition. Future studies should further explore the mechanisms underlying the size effects of the typical soils on particle interactions, coagulation, and transport behaviors under environmentally relevant conditions.

Acknowledgments

This work was supported by Natural Science Foundation of Shaanxi Province (2023-JC-YB-263) and the National Natural Science Foundation of China (41701261), and the Fundamental Research Funds for the Central Universities (2452020165).

Author Contributions

Conceptualization, Xu, C.Y., Geng, Z.C., and Hu, F.N.; methodology, Xu, C.Y.; software, Yan, Y.Y.; formal analysis, Liu, J.J.; investigation, Zhang, X.R.; resources, Yan, Y.Y.; writing—original draft, Yan, Y.Y.; writing—review and editing, Xu, C.Y., and Hu, F.N.; visualization, Xu, C.Y., and Yan, Y.Y.; funding acquisition, Xu, C.Y., Geng, Z.C. and Hu, F.N.. All authors have read and agreed to the published version of the manuscript.

Declaration of Interest Statement

The authors declare that they have no known competing financial interests or personal relationships that could have appeared to influence the work reported in this paper.

463

References

465 Audette, Y., Congreves, K.A., Schneider, K., Zaro, G.C., Nunes, A.L.P., Nunes, A.L.P.,

466 Zhang, H.J., Voroney, R.P.: The effect of agroecosystem management on the

467 distribution of C functional groups in soil organic matter: A review. Biol. Fertil.

468 Soils. 57, 881–894, 2021.

469 Baalousha, M.: Aggregation and disaggregation of iron oxide nanoparticles: Influence

470 of particle concentration, pH and natural organic matter. Sci. Total Environ. 407(6),

471 2093–2101, 2009.

472 Baalousha, M.: Effect of nanomaterial and media physicochemical properties on

473 nanomaterial aggregation kinetics. NanoImpact. 6, 55–68, 2017.

474 Cárdenas, J.P., Santiago, A., Tarquis, A.M., Losada, J.C., Borondo, F., Benito, R.M.:

475 Soil porous system as heterogeneous complex network. Geoderma. 160(1), 13–21,

476 2010.

477 Chen, K.L., Elimelech, M.: Aggregation and deposition kinetics of Fullerene (C_{60})

478 nanoparticles. Langmuir 22, 10994–11001, 2006.

479 Chenu, C., Plante, A.F.: Clay-sized organo-mineral complexes in a cultivation

480 chronosequence: revisiting the concept of the'primary organo-mineral complex'.

481 Eur J Soil Sci. 57(4), 596–607, 2006.

482 Ding, W., Liang, H.X., Zhang, H.W., Sun, H., Geng, Z.C., Xu, C.Y.: A

483 cellulose/bentonite grafted polyacrylic acid hydrogel for highly-efficient removal

484 of Cd(II). J. Water Process. Eng. 51, 103414, 2023.

485 Dong, S.N., Zeng, Z., Cai, W.W., Zhou, Z.Y., Dou, C.B., Liu, H., Xia, J.H.: The zeta

486 potentials of g-C$_3$N$_4$ nanoparticles: Effect of electrolyte, ionic strength, pH, and

487 humic acid. J. Nanopart Res. 21, 233, 2019.

488 Filella, M., Zhang, J.W., Newman, M.E., Buffle, J.: Analytical applications of photon

489 correlation spectroscopy for size distribution measurements of natural colloidal

490 suspensions: capabilities and limitations. Colloid Surf. A. 120(1–3), 27–46, 1997.

491 He, Y.T., Wan, J., Tokunaga, T.: Kinetic stability of hematite nanoparticles, The effect

492 of particle sizes. J. Nanopart Res. 10, 321–332, 2008.

493 Hou, J., Li, H., Zhu, H.L.,Wu, L.S.: Determination of clay surface potential, a more

494 reliable approach. Soil Sci Soc Am J. 73(5), 1658–1663, 2009.

495 Hsu, J.P., Kuo, Y.C.: An Extension of the Schulze-Hardy Rule to Asymmetric

496 Electrolytes. J. Colloid Interface Sci. 171(1), 254–255, 1995.

497 Hu, N., Xu, C.Y., Geng, Z.C., Hu, F.N., Li, Q.R., Ma, R.T., Wang, Q.: The interplay of

498 particle properties and solution chemistry on aggregation kinetics of soil

499 nanoparticles. J Soils Sediments. 22, 1761–1772, 2022.

500 IUSS Working Group WRB. World Reference Base for Soil Resources. International

501 soil classification system for naming soils and creating legends for soil maps. 4th

502 edition. International Union of Soil Sciences (IUSS), Vienna, Austria. 2022.

503 Jiang, C.L., Séquaris, J.M., Vereecken, H., Klumpp, E.: Effects of inorganic and organic

504 anions on the stability of illite and quartz soil colloids in Na-, Ca- and mixed Na-

505 Ca systems. Colloids Surf. A. 415, 134–141, 2012.Lead, J.R., Wilkinson, K.J.:

506 Aquatic Colloids and Nanoparticles: Current Knowledge and Future Trends.

507   Environ. Chem. 3(3), 159–171, 2006.

508   Li, S.X., Luo, Y.M., Zhang, H.B., Huang, Y.J., Li, Z., Wei, J.: Arsenic forms in various

509   particle-size fractions of red soil-Chemical fractionation and speciation using

510   XANES analysis. Acta Scientiae Circumstantiae. 31(12), 2733–2739, 2011.

511   Li, W. Y., Zhu, X.Y., He, Y., Xing, B. S., Xu, J.M.: Enhancement of water solubility and

512   mobility of phenanthrene by natural soil nanoparticles. Environ Pollut. 176, 228–

513   233, 2013.

514   Liang, H.X., Sun, R.R., Song, B., Sun, Q.Q., Peng, P., She, D.: Preparation of nitrogen-

515   doped porous carbon material by a hydrothermal-activation two-step method and

516   its high-efficiency adsorption of Cr(VI). J. Hazard. Mater. 387, 121987, 2020.

517   Liu, G., Zheng, H., Jiang, Z., Zhao, J., Wang, Z., Pan, B., Xing, B.: Formation and

518   physicochemical characteristics of nano biochar: insight into chemical and

519   colloidal stability. Environ. Sci. Technol. 52(18), 10369–10379, 2018.Luo, J.J.,

520   Niu, Q., Jin, M.C., Cao, Y.A., Ye, L.R., Du, R.P.: Study on the effects of oxygen-

521   containing functional groups on Hg^0 adsorption in simulated flue gas by XAFS

522   and XPS analysis. J. Hazard. Mater. 376(15), 21–28, 2019.

523   Mashayekhi, H., Ghosh, S., Du, P., Xing, B.: Effect of natural organic matter on

524   aggregation behavior of C60 fullerene in water. J. Colloid Interf. Sci. 374(1), 111–

525   117, 2012.

526   Mayordomo, N., Degueldre, C., Alonso, U., Missana, T.: Size distribution of FEBEX

527   bentonite colloids upon fast disaggregation in low-ionic strength water. Clay

528   Miner. 51(2), 213–222, 2016.

529   Meng, Z.Y., Hashmi, S.M., Elimelech, M.: Aggregation rate and fractal dimension of

530   fullerene nanoparticles via simultaneous multiangle static and dynamic light

531   scattering measurement. J. Colloid Interface Sci. 392, 27–33, 2013.

532   Moayedi, H., Kazemian, S.: Zeta potentials of suspended humus in multivalent cationic

533   saline solution and its effect on electro-osomosis behavior. J. Dispers Sci. Technol.

534   34(2), 283–294, 2013.

535   Said-Pullicino, D., Giannetta, B., Demeglio, B., Missong, A., Gottselig, N., Romani,

536   M., Bol, R., Klumpp, E., Celi, L.: Redox-driven changes in water-dispersible

537   colloids and their role in carbon cycling in hydromorphic soils. Geoderma. 385,

538   114894, 2021.

539   Schäfer, T., Huber, F., Seher, H., Missana, T., Alonso, U., Kumke, M., Eidner, S., Claret,

540   F., Enzmann, F.: Nanoparticles and their influence on radionuclide mobility in

541   deep geological formations. Appl. Geochemistry. 27(2), 390–403, 2012.

542   Song, B.Q., Chen, M., Zhao, L., Qiu, H., Cao, X.D.: Physicochemical property and

543   colloidal stability of micron- and nano-particle biochar derived from a variety of

544   feedstock sources. Sci. Total Environ. 661, 685–695, 2019.

545   Sun, Y.L., Pan, D.Q., Wei, X.Y., Xian, D.F., Wang, P., Hou, J.J.: Insight into the stability

546   and correlated transport of kaolinite colloid: Effect of pH, electrolytes and humic

547   substances. Environ. Pollut. 266, 115189, 2020.

548   Tan, Z.X., Yuan, S.N., Hong, M.F., Zhang, L.M., Huang, Q.Y.: Mechanism of negative

549   surface charge formation on biochar and its effect on the fixation of soil Cd. J.

550   Hazard. Mater. 384, 121370, 2019.

Tang, Y., Li, H., Liu, X.M., Zhu, H.L., Tian, R.: Unraveling the size distributions of surface properties for purple soil and yellow soil. J Environ Sci (China). 32, 81–89, 2015.

Tsao, T.M., Chen, Y.M., Sheu, H., Tzou, Y.M., Chou, Y.M., Wang, M.K.: Separation and identification of soil nanoparticles by conventional and synchrotron X-ray diffraction. Appl. Clay Sci. 85, 1–7, 2013.

Tsao, T.M., Chen, Y.M., Wang, M.K., Huang, P.M.: Structural transformation and physicochemical properties of environmental nanoparticles by comparison of various particle-size fractions. Soil Sci Soc Am J. 75(2), 533–541, 2011.

Wang, L.F., Wang, L.L., Ye, X.D., Li, W.W., Ren, X.M., Sheng, G.P., et al.: Coagulation kinetics of humic aggregates in mono-and divalent electrolyte solutions. Environ. Sci. Technol. 47(10), 5042–5049, 2013.

Wang, Q.R., Li, Y.C., Wang, Y.: Optimizing the weight loss-on-ignition methodology to quantify organic and carbonate carbon of sediments from diverse sources. Environ. Monit. Assess. 174, 241–257, 2011.

Wei, X.Y., Pan, D.Q., Xu, Z., Xian, D.F., Li, X.L., Tan, Z.Y., Liu, C.L., Wu, W.S.: Colloidal stability and correlated migration of illite in the aquatic environment: The roles of pH, temperature, multiple cations and humic acid. Sci. Total Environ. 768, 144174, 2021.

Weil, R.R., Brady, N.C.: The Nature and Properties of Soils, Global Edition. Pearson Education Limited. 2016.

Weissenberger, G., Henderikx, R.J., Peters, P.J.: Understanding the invisible hands of

573   sample preparation for cryo-EM. Nat. Methods. 18(5), 463–471, 2021.

574   Wilson, M. A., Tran, N. H., Milev, A. S., Kannangara, G. S. K., Volk, H.: Nanomaterials

575   in soils. Geoderma. 146, 291–302, 2008.

576   Won, J., Burns, S.E.: Role of Immobile Kaolinite Colloids in the Transport of Heavy

577   Metals. Environ. Sci. Technol. 52(5): 2735–2741, 2018.

578   Xu, C.Y., Deng, K.Y., Li, J.Y., Xu, R.K.: Impact of environmental conditions on

579   aggregation kinetics of hematite and goethite nanoparticles. J. Nanopart Res. 17,

580   394, 2015.

581   Xu, C.Y., Li, Q.R., Geng, Z.C., Hu, F.N., Zhao, S.W.: Surface properties and suspension

582   stability of low–temperature pyrolyzed biochar nanoparticles: Effects of solution

583   chemistry and feedstock sources. Chemosphere. 259, 127510, 2020a.

584   Xu, C.Y., Xu, R.K., Li, J.Y., Deng, K.Y.: Phosphate-induced aggregation kinetics of

585   hematite and goethite nanoparticles. J. Soils Sediments. 17, 352–363, 2017.

586   Xu, C.Y., Zhou, T.T., Wang, C.L., Liu, H.Y., Zhang, C.T., Hu, F.N., Zhao, S.W., Geng,

587   Z.C.: Aggregation of polydisperse soil colloidal particles: Dependence of

588   Hamaker constant on particle size. Geoderma. 359, 113999, 2020b.

589   Xu, Z., Pan, D.Q., Sun, Y.L., Wu, W.S.: Stability of GMZ bentonite colloids:

590   Aggregation kinetic and reversibility study. Appl. Clay Sci. 161, 436–443. 2018.

591   Yin, X.Q., Gao, B., Ma, L.Q., Saha, U.K., Sun, H.M., Wang, G.D.: Colloid-facilitated

592   Pb transport in two shooting-range soils in Florida. J. Hazard. Mater. 177(1–3),

593   620–625, 2010.

594   Yu, X., Fu, Y., Lu, S.: Characterization of the pore structure and cementing substances

595   of soil aggregates by a combination of synchrotron radiation X-ray micro–

596   computed tomography and scanning electron microscopy. Eur. J. Soil Sci. 68(1),

597   66–79, 2017.

598 Zhang, Q., Bol, R., Amelung, W., Missong, A., Siemens, J., Mülder, I.: Water

599   dispersible colloids and related nutrient availability in Amazonian Terra Preta soils.

600   Geoderma. 397, 115103, 2021.

601 Zhang, Z.Y., Huang, L., Liu, F., Wang, M.K., Fu, Q.L., Zhu, J.: Characteristics of clay

602   minerals in soil particles of two Alfisols in China. Appl. Clay Sci. 120, 51–60,

603   2016.

604 Zhou, D.X., Ji, Z.X., Jiang, X.M., Dunphy, D.R., Brinker, J., Keller A.A.: Influence of

605   material properties on TiO_2 nanoparticle agglomeration. PLoS One. 8(11), e81239,

606   2013.

607 Zhu, X., Chen, H., Li, W., He, Y., Brookes, P.C., Xu, J.: Aggregation kinetics of natural

608   soil nanoparticles in different electrolytes. Eur. J. Soil Sci. 65(2), 206–217, 2014.

609
610

611 **Table captions**

612 **Table 1** The average diameters and distribution patterns of soil colloids.

613 **Table 2** The physiochemical properties of soil colloids.

614 **Table 3** The dominant clay minerals of soil colloidal fractions (shown in mass

615 fraction, %).

616 **Table 4** The aggregation rates of soil colloids.

617

618   **Table 1** The average diameters and distribution patterns of soil colloids

Soil type	Colloidal fractions	Number-weighted diameter (nm)	Intensity-weighted diameter (nm)	D_{10} (nm)	D_{90} (nm)
Anthrosol	$d < 2$ µm	133.16 ± 24.28	396.81 ± 12.34	71.53	232.49
	$d < 1$ µm	127.84 ± 20.29	371.45 ± 11.88	67.64	219.87
	$d < 100$ nm	72.47 ± 7.04	294.10 ± 15.80	38.74	136.72
Calcisol	$d < 2$ µm	141.23 ± 24.33	439.20 ± 12.72	78.29	244.97
	$d < 1$ µm	131.67 ± 15.77	372.07 ± 8.23	75.84	231.64
	$d < 100$ nm	85.48 ± 16.93	312.25 ± 33.58	47.84	158.99

619   Note: D_{10}, D_{50} and D_{90} represent diameter of particles with a cumulative distribution of 10%, 50% and
620   90%, respectively.

621

622

Table 2 The physiochemical properties of soil colloids

Soil type	Colloidal fractions	Yield (%)	Total carbon content (g·kg⁻¹)	Organic carbon content (g·kg⁻¹)	CaCO₃ content (g·kg⁻¹)	Specific surface area (m²·g⁻¹)
Anthrosol	$d < 2$ μm	25.12	20.90 ± 0.30	10.90 ± 1.29	10.00	65.37
	$d < 1$ μm	18.76	20.65 ± 0.15	10.91 ± 0.43	9.74	72.99
	$d < 100$ nm	6.32	58.25 ± 0.35	27.38 ± 0.21	30.87	45.28
Calcisol	$d < 2$ μm	23.17	24.00 ± 0.30	11.66 ± 0.60	12.34	49.99
	$d < 1$ μm	16.20	22.30 ± 0.20	12.76 ± 0.11	9.54	61.88
	$d < 100$ nm	4.70	76.30 ± 0.40	28.31 ± 0.15	47.99	34.53

623

624   **Table 3** The dominant clay minerals of soil colloidal fractions (shown in mass fraction, %)

Soil type	Colloidal fractions	Illite	Kaolinite	Chlorite	Vermiculite
	$d < 2$ μm	34	23	4	9
Anthrosol	$d < 1$ μm	30	22	7	11
	$d < 100$ nm	37	14	16	3
	$d < 2$ μm	24	22	29	16
Calcisol	$d < 1$ μm	31	19	25	12
	$d < 100$ nm	37	16	17	5

625

Table 4 The aggregation rates of soil colloids

Soil type	Colloidal fractions	Aggregation rate		Fractal dimension	
		In 50 mmol·L^{-1} NaCl (nm·min^{-1})	In 1 mmol·L^{-1} CaCl$_2$ (nm·min^{-1})	Na	Ca
Anthrosol	$d < 2$ μm	19.46	12.01	1.69 ± 0.19	1.33 ± 0.26
	$d < 1$ μm	14.91	11.48	1.75 ± 0.06	1.52 ± 0.19
	$d < 100$ nm	7.72	9.97	1.71 ± 0.26	1.68 ± 0.13
Calcisol	$d < 2$ μm	8.98	8.22	1.30 ± 0.17	1.36 ± 0.17
	$d < 1$ μm	7.15	7.33	1.71 ± 0.24	1.30 ± 0.31
	$d < 100$ nm	3.95	5.22	1.52 ± 0.22	1.58 ± 0.19

627

628 **Figure captions**

629 **Fig. 1.** The photoelectron spectrum C1s and O1s peak diagram of Anthrosol and

630 Calcisol colloids. C1s of Anthrosol colloids, a. $d < 2$ μm, b. $d < 1$ μm, c. $d < 100$ nm;

631 C1s of Calcisol colloids, d. $d < 2$ μm, e. $d < 1$ μm, f. $d < 100$ nm; O1s of Anthrosol

632 colloids, g. $d < 2$ μm, h. $d < 1$ μm, i. $d < 100$ nm; O1s of Calcisol colloids, j. $d < 2$ μm,

633 k. $d < 1$ μm, l. $d < 100$ nm.

634 **Fig. 2.** The zeta potential of Anthrosol (a) and Calcisol (b) colloids of $d < 2$ μm, < 1 μm,

635 and < 100 nm at different pH

636 **Fig. 3.** The CCCs of Anthrosol (a) and Calcisol (b) colloids of $d < 2$ μm, < 1 μm, and $<$

637 100 nm in NaCl solution

638 **Fig. 4.** The CCC of Anthrosol (a) and Calcisol (b) colloids of $d < 2$ μm, < 1 μm, and $<$

639 100 nm in CaCl2 solution
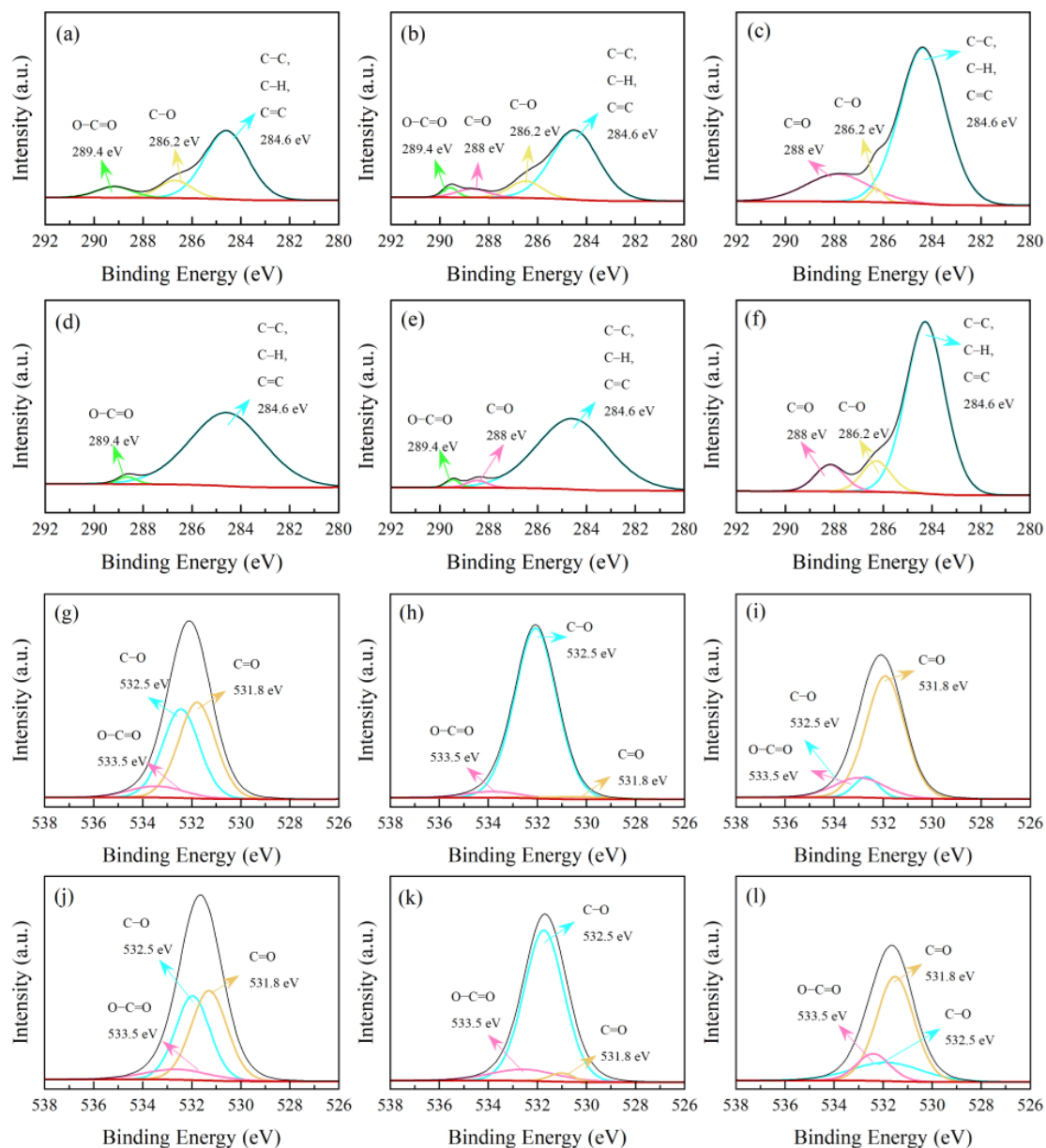
Fig. 1 The photoelectron spectrum C1s and O1s peak diagram of Anthrosol and Calcisol colloids. C1s of Anthrosol colloids, (a). d < 2 μm, (b). d < 1 μm, (c). d < 100 nm; C1s of Calcisol colloids, (d). d < 2 μm, (e). d < 1 μm, (f). d < 100 nm; O1s of Anthrosol colloids, (g). d < 2 μm, (h). d < 1 μm, (i). d < 100 nm; O1s of Calcisol colloids, (j). d < 2 μm, (k). d < 1 μm, (l). d < 100 nm.
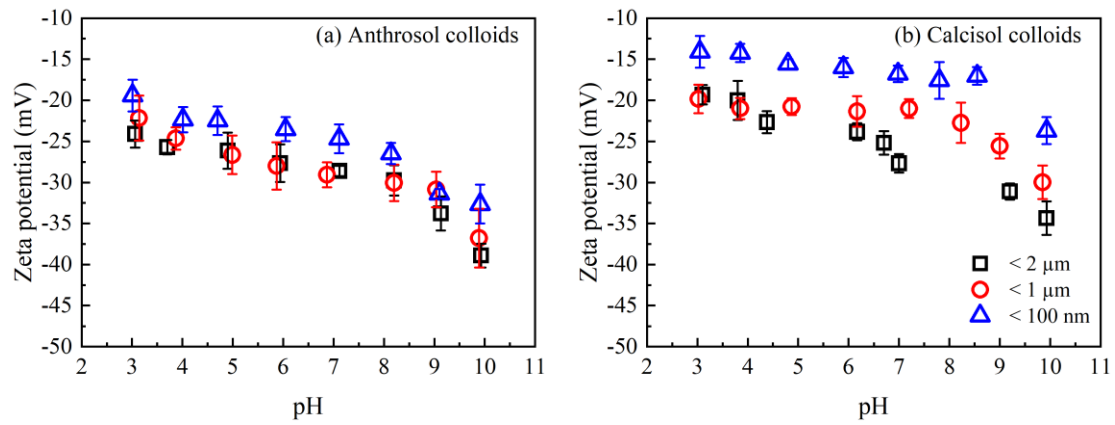
647

Fig. 2 The zeta potential of Anthrosol (a) and Calcisol (b) colloids of d < 2 μm, < 1 μm, and < 100 nm at different pH

650
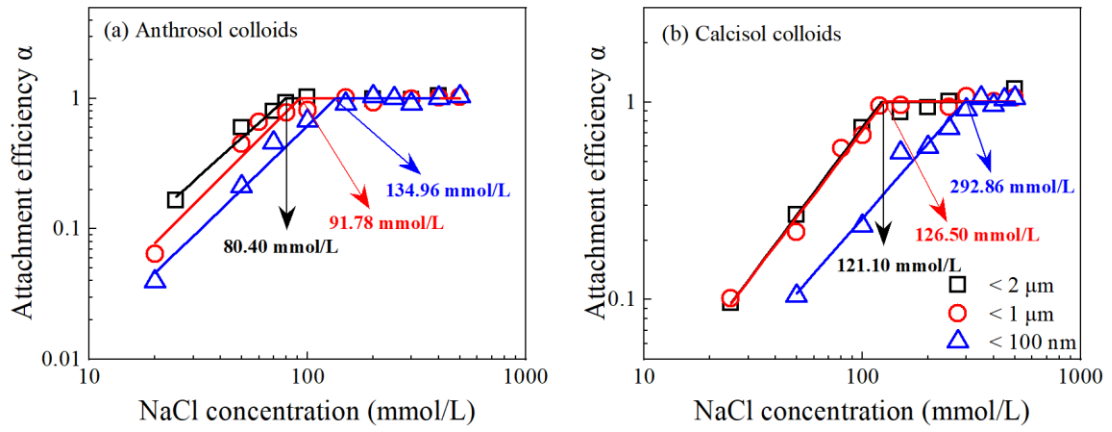
Fig. 3 The CCCs of Anthrosol (a) and Calcisol (b) colloids of d < 2 μm, < 1 μm, and < 100 nm in NaCl solution
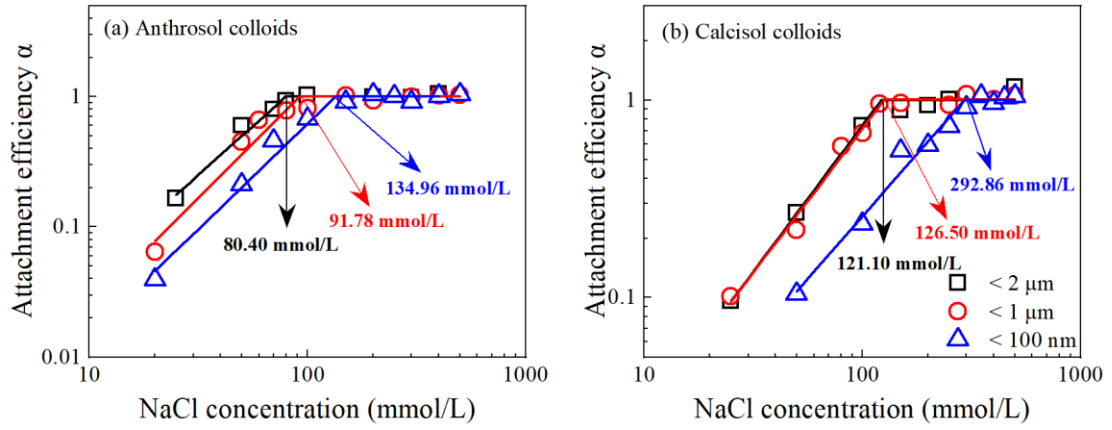
656

657 **Fig. 4** The CCC of Anthrosol (a) and Calcisol (b) colloids of *d* < 2 μm, < 1 μm, and < 100 nm

658 in CaCl₂ solution。